Electronic Supplementary Material (ESI) for Nanoscale.

Supplementary Information for:

Full-spectrum photocatalyst with strong near-infrared photoactivity derived from synergy of nano-heterostructured Er^{3+}-doped multi-phase oxides

Huabin Chen,[a] Wenxia Liu,[a]* Bin Hu,[a] Zhuozhuo Qin[a] and Hong Liu[b]
[a] *Key Laboratory of Pulp&Paper Science and Technology (Qilu University of Technology), Ministry of Education, Jinan, Shandong 250353, China*
[b] *State Key Laboratory of Crystal Materials, Shandong University, Jinan, Shandong 250100, China.*
Correspondence o: W. Liu (E-mail: liuwenxia@qlu.edu.cn)

1. Self-assembled experimental device for photodegradation of MO under NIR light irradiation

Fig. S1. Device for NIR photocatalytic experiment

The device for photocatalytic test under NIR light irradiation is composed of a 6.5 W NIR LED light with a maximum emission at 850 nm, a 100 ml glass beaker covered with tinfoil, a water-bath with cooling water and magnetic stirrer with beaker stand and clamp.

2. N_2 adsorption-desorption isotherm of Er^{3+}-doped Zn/Cu/Al-MPO and Zn/Cu/Al-MPO

The N_2 adsorption–desorption isotherms of MPO samples were used to characterize the textural property of the MPO samples and measured with a Micomeritics ASAP2020 surface analyzer. The specific surface areas of the samples were calculated by the Brunauer–Emmett–Teller (BET) technique from their N_2 adsorption isotherms, and their pore size distributions were determined by their desorption isotherms using the Barrett–Joiner–Halenda (BJH) method.

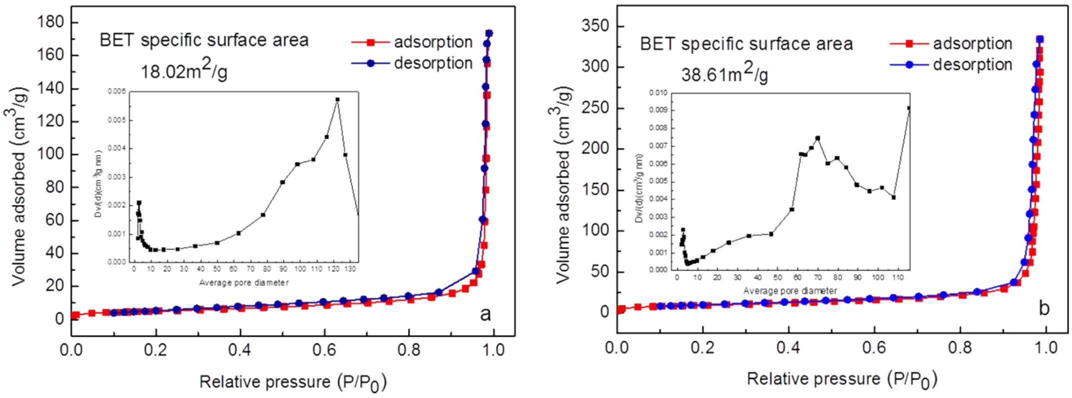

Fig. S2. N_2 adsorption-desorption isotherms of (a) Zn/Cu/Al-MPO and (b) Er^{3+}-doped Zn/Cu/Al-MPO. Insets are the corresponding pore size distribution curves calculated from the desorption branches.

The Zn/Cu/Al-MPO and Er^{3+}-doped Zn/Cu/Al-MPO show nitrogen adsorption–desorption isotherms of type IV with a small hysteresis loop of type H3 [14], as shown in Fig. S2, indicating that plate-like particles still occur in the calcined samples. The sample Er^{3+}-doped Zn/Cu/Al-MPO present a larger BET specific surface area (38.61m^2/g) than ZnCuAl-MPO (18.02m^2/g). It is common that the surface area of multi-phase oxides (MPO) from HLC decreases with elevating temperature owing to the increase of crystallinity. In our cases, the doped Er not only reduces the crystallinity of the HLC precursor, but also restrains the formation of the spinel $ZnAl_2O_4$, resulting in the lower crystallinity (Fig.1) and thus higher specific surface area of Er^{3+}-doped Zn/Cu/Al-MPO than that of Zn/Cu/Al-MPO. From the pore size distribution curves shown in the insets in Fig. S2, it is found that the Zn/Cu/Al-MPO have macropores with diameters around 100 nm, while the Er^{3+}-doped Zn/Cu/Al-MPO possesses both mesopores and macropores with a diameter of about 40 and 70 nm. The larger specific surface area and mesopores of the Er^{3+}-doped Zn/Cu/Al-MPO would promote the adsorption of dye molecules, possibly leading to a better catalytic activity.

3. EDS of Er^{3+}-doped Zn/Cu/Al-MPO

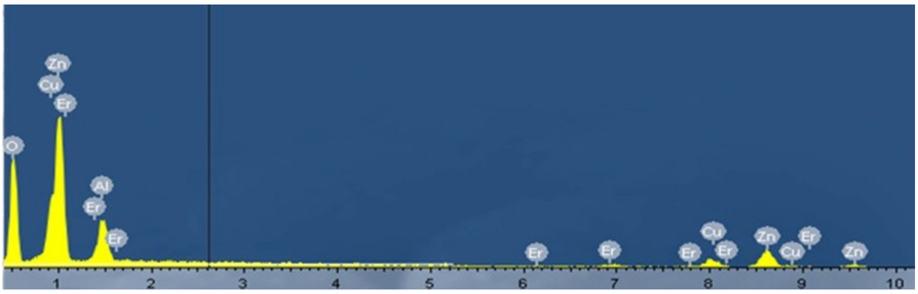

Fig. S3. Energy-dispersive x-ray spectrum (EDS) of Er^{3+}-doped Zn/Cu/Al-MPO

An energy-dispersive X-ray spectrometer (EDS) attached to the FE-SEM (Hitachi S-4800) was used to investigate the chemical composition of Er^{3+}-doped Zn/Cu/Al-MPO. From Fig. S3, the energy-dispersive x-ray spectrum (EDS), one can find that the Er^{3+}-doped Zn/Cu/Al-MPO consists of oxygen, zinc, copper, aluminum and erbium.

4. HRTEM images of Er^{3+}-doped Zn/Cu/Al-MPO with heterostructures among Er^{3+}-doped ZnO, Er^{3+}-doped CuO, and Er^{3+}-doped $ZnAl_2O_4$

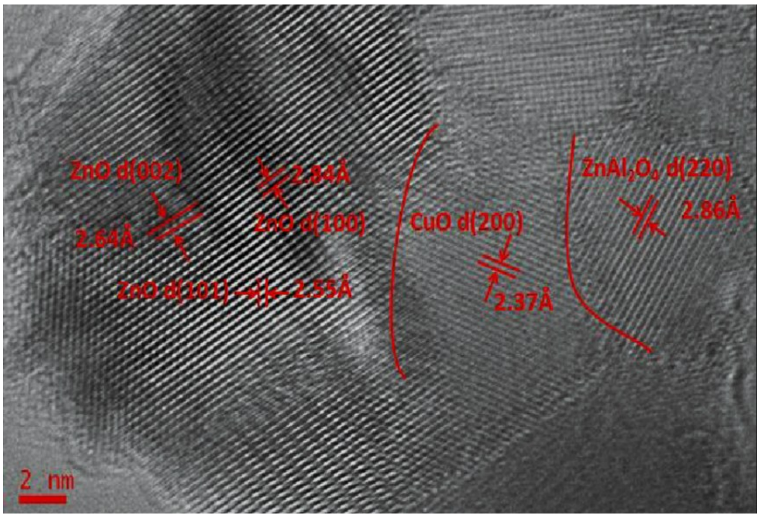

Fig. S4. HRTEM images of Er^{3+}-doped Zn/Cu/Al-MPO with heterostructures

Fig. S4 shows that Er^{3+}-doped ZnO, Er^{3+}-doped CuO, and Er^{3+}-doped $ZnAl_2O_4$ simultaneously occur in the Er^{3+}-doped Zn/Cu/Al-MPO. The interface and transition of lattice fringes among the ZnO, CuO and $ZnAl_2O_4$ directly evidenced that heterojunctions are formed among different metal oxide phases.

5. XPS spectra of Zn/Cu/Al-MPO and Er^{3+}-doped Zn/Cu/Al-MPO

To evaluate the effect of Er on the surface composition and chemical state of Zn/Cu/Al-MPO, X-ray photoelectron spectrometry (XPS) measurements were carried out for both Er^{3+}-doped Zn/Cu/Al-MPO and Zn/Cu/Al-MPO. The XPS spectra were recorded on an ESCALAB 250 photoelectron spectrometer. All of the binding energies were calibrated by the C1s peak at 284.6 eV. In the survey XPS spectra shown in Fig. S5a, Er can be found on the Er^{3+}-doped Zn/Cu/Al-MPO surface, and Zn, O, Cu, Al and C on both of the two sample surfaces, confirming the doping of Er in the Er^{3+}-doped Zn/Cu/Al-MPO, and the high purity of the samples. The C1s peak at 284.6 eV is attributed to an adventitious carbon-based contaminant, and was used to calibrate the binding energies of the other elements. The molar ratio of Zn:Cu:Al for Zn/Cu/Al-MPO and Zn:Cu:Al:Er for Er^{3+}-doped Zn/Cu/Al-MPO are 15.3:3.0:28.4 and 14.1:3.9:23.6:1.3, respectively. The unusual high ratios of Al indicate the enrichment of $ZnAl_2O_4$ on the surfaces of Zn/Cu/Al-MPO and Er^{3+}-doped Zn/Cu/Al-MPO. However, the introduction of Er may suppress the migration of $ZnAl_2O_4$ to the Er^{3+}-doped Zn/Cu/Al-MPO surface, enhancing the percentage of CuO on the Er^{3+}-doped Zn/Cu/Al-MPO surface. In the high-resolution spectrum of Er 4d in the Er^{3+}-doped Zn/Cu/Al-MPO, shown in Fig. S5b, the peak of Er $4d_{5/2}$ is located at 168.0 eV, corresponding to the trivalent state of

Er.[1,2]

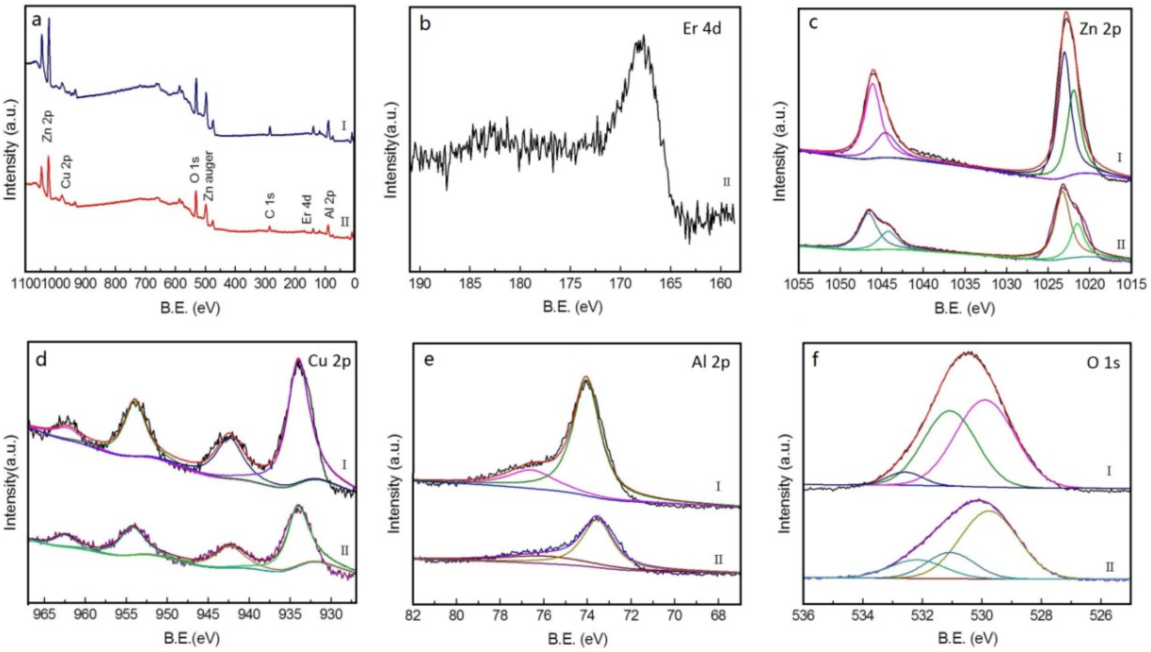

Fig. S5. (a) XPS fully scanned spectra of (I) Zn/Cu/Al-MPO and (II) Er^{3+}-doped Zn/Cu/Al-MPO; (b) Er 4d, (c) Zn 2p, (d) Cu 2p, (e) Al 2p and (f) O 1s core-level XPS spectra of (I) Zn/Cu/Al-MPO and (II) Er^{3+}-doped Zn/Cu/Al-MPO.

In the core-level XPS spectrum of Zn 2p from Zn/Cu/Al-MPO shown in Fig. S5c, the binding energy peaks assigned to Zn $2p_{1/2}$ and Zn $2p_{3/2}$ can each be deconvoluted into two peaks: two Zn $2p_{1/2}$ peaks at binding energies of 1046.1 eV and 1044.5 eV, as well as two Zn $2p_{3/2}$ peaks at binding energies of 1023.0 and 1021.9 eV. The two main peaks at the binding energies of 1046.1 and 1023.0 eV are assigned to Zn $2p_{1/2}$ and Zn $2p_{3/2}$ of octahedral Zn^{2+} in $ZnAl_2O_4$, while the other two peaks at the binding energies of 1044.5 eV and 1021.9 eV are assigned to the Zn $2p_{1/2}$ and Zn $2p_{3/2}$ of tetrahedral Zn^{2+} in ZnO.[3,4] This observation further proves the occurrence of ZnO and $ZnAl_2O_4$ in the Zn/Cu/Al-MPO sample, and more concentrated $ZnAl_2O_4$ occurrence on the surfaces of Zn/Cu/Al-MPO. For Er^{3+}-doped Zn/Cu/Al-MPO, the binding energies of Zn $2p_{1/2}$ and Zn $2p_{3/2}$ for tetrahedral Zn^{2+} in ZnO shift to 1044.2 eV and 1021.5 eV, while those for octahedral Zn^{2+} in $ZnAl_2O_4$ shift to 1046.6 and 1023.3 eV, respectively, indicating changed chemical environments surrounding Zn^{2+} in both ZnO and $ZnAl_2O_4$ compared to Zn/Cu/Al-MPO due to the doping of Er^{3+}. However, octahedral Zn^{2+} in $ZnAl_2O_4$ is still the dominant Zn^{2+} on the surfaces of Er^{3+}-doped Zn/Cu/Al-MPO.

The expanded XPS spectra of Zn/Cu/Al-MPO and Er^{3+}-doped Zn/Cu/Al-MPO from 925 eV to 970 eV (Fig. S5d) show similar Cu 2p peaks, which include two main symmetric peaks assigned to Cu $2p_{3/2}$ and Cu $2p_{1/2}$ at 934.0 eV and 954.0 eV for Zn/Cu/Al-MPO, and at 934.0 eV and 954. 2 eV for Er^{3+}-doped Zn/Cu/Al-MPO, as well as their satellite peaks at 942.3 eV and 962.3 eV for Zn/Cu/Al-MPO, and at 942.4 eV and 962.5 eV for Er^{3+}-doped Zn/Cu/Al-MPO. This observation is consistent with those reported for CuO,[5] clearly indicative of the occurrence of Cu as CuO in both Zn/Cu/Al-MPO and Er^{3+}-doped Zn/Cu/Al-MPO. The slightly higher binding energy of Cu 2p in Er^{3+}-doped Zn/Cu/Al-MPO than that in Zn/Cu/Al-MPO implies the effect of Er^{3+} doping on CuO in Er^{3+}-doped Zn/Cu/Al-MPO. In the core-level XPS spectrum of Al 2p for Zn/Cu/Al-MPO, shown in Fig. S5e, the Al 2p peak is asymmetric and can be deconvoluted into a very weak peak at the binding energy of 76.6 eV and a strong peak at the binding energy of 74.1 eV. The stronger peak at lower binding energy is assigned to Al^{3+} in O-Al-O bonds from $ZnAl_2O_4$, while the weaker peak at higher binding energy is assigned to Al-OH bonds from hydrated O-Al-O bonds.[6] The corresponding Al 2p peaks assigned to Al^{3+} in O-Al-O and in Al-OH shift to lower binding energy of 76.1 eV and 73.6 eV, respectively, for Er^{3+}-doped Zn/Cu/Al-MPO (Fig. S5d) due to Er^{3+} ions with greater radius and lower electronegativity incorporating into the $ZnAl_2O_4$ crystal structure, resulting in electron cloud density rearrangement on the O orbital.[7] Meanwhile, the doping of Er^{3+} in Zn/Cu/Al-MPO also leads to the variation of O1s core-level XPS spectrum of Zn/Cu/Al-MPO after deconvolution. As shown in Fig. S5f, among the three O 1s peaks of Zn/Cu/Al-MPO at binding energies of 532. 6, 531.1 and 529.9 eV, only the binding energy of O 1s peak that represents oxygen in oxygen deficient regions at 531.1 eV [8] remains unchanged. However, its relative strength is reduced. The binding energies of O 1s peaks that represent absorbed oxygen on sample surfaces and lattice oxygen from various metal oxides [8] shift to lower binding energies of 532. 2 and 529.7 eV, respectively, due to lattice expansion of $ZnAl_2O_4$ caused by the larger size of Er^{3+}, compared to Al^{3+} (Fig. 1). The lattice oxygen even becomes the dominant oxygen in the Er^{3+}-doped Zn/Cu/Al-MPO because of the reduction of oxygen in oxygen deficient regions.

6. Photodegradation of MO under the irradiation of UV and NIR lights

Fig. S6 shows the photocatalytic degradation of MO with a concentration of 20 mg/L in the presence of Er^{3+}-doped Zn/Cu/Al-MPO (20mg) under UV and near-infrared light irradiations. As shown in Fig. S6, the Er^{3+}-doped Zn/Cu/Al-MPO show very strong adsorption capacity in the dark, which results in the quick removal of MO. Under the irradiations of UV and NIR lights, the removal rate of MO is further improved, confirming the UV and NIR photocatalytic activity of the Er^{3+}-doped Zn/Cu/Al-MPO. The removal rate of MO is as high as 91% under 80 min NIR irradiation. However, the difference between the photodegradation and adsorption rates is too small to persuasively characterize the photocatalytic activity.

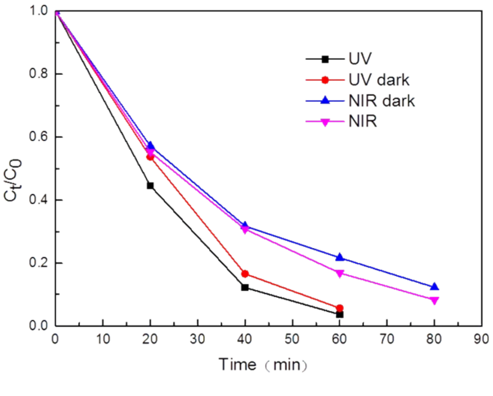

Fig. S6. Photocatalytic degradation of MO with a concentration of 20 mg/L in the presence of Er^{3+}-doped Zn/Cu/Al-MPO (20mg) under UV and near-infrared light irradiations.

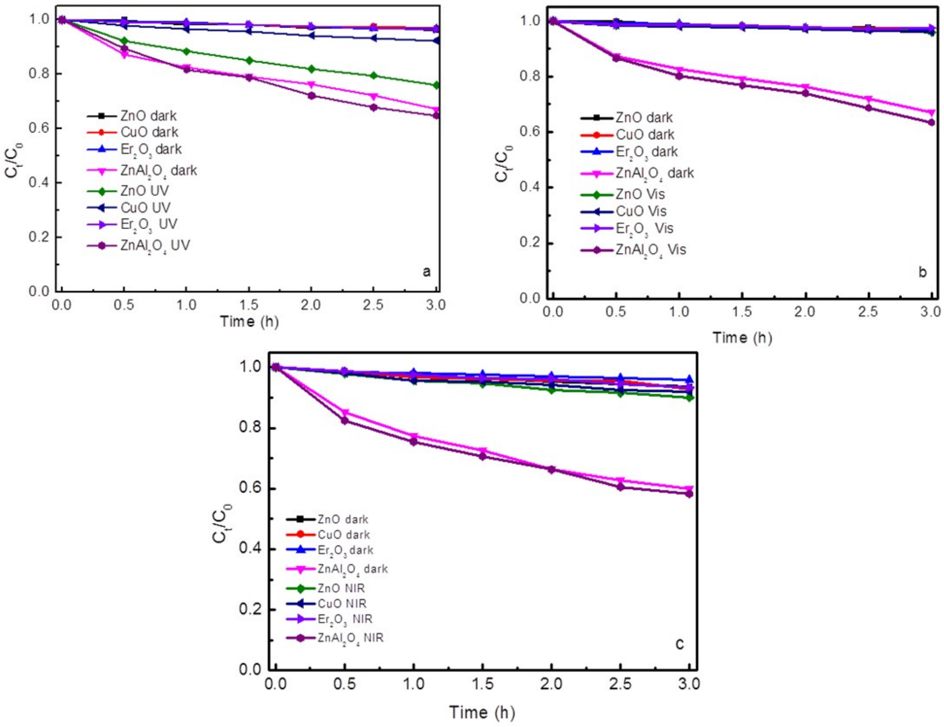

Fig. S7. Photocatalytic degradation of MO with a concentration of 20 mg/L in the presence of ZnO, CuO, Er_2O_3 and $ZnAl_2O_4$ under the irradiation of (a) UV, (b) visible and (c) NIR lights.

Fig. S7 shows the photocatalytic degradation of MO with a concentration of 20 mg/L in the presence of ZnO, CuO, Er_2O_3 and $ZnAl_2O_4$ under the irradiation of UV, visible and NIR lights. As shown in Fig. S6, ZnO nanoparticles show considerable UV photocatalytic activity on degradation of MO. CuO nanoparticles only display very weak UV photocatalytic activity while Er_2O_3 nanoparticles have not any photoactivity on degradation of MO. All of the ZnO, CuO, Er_2O_3 hardly show any visible and NIR photoactivity. The $ZnAl_2O_4$ nanoparticles have a considerable adsorption for MO, and show a weak UV photoactivity. Considering $ZnAl_2O_4$ nanoparticles have no absorption at visible and NIR regions, the removal of MO under visible and NIR irradiation is ascribed to adsorption. CuO is a narrow band gap semiconductor with optical absorption extending to NIR region.[9] Its low photocatalytic activity must be ascribed to its low carrier mobility, which is adverse to the transfer of charge carriers.

7. Comparison of NIR photocatalytic activity between Er^{3+}-doped Zn/Cu/Al-MPO and the other full spectrum photocatalysts

Table S1 list the NIR photoactivities of various reported full spectrum photocatalysts. Since the NIR light sources, charge amounts of catalyst, MO and the concentration of MO are different from that we used in the photocatalytic experiment, it is hard to give a direct comparison for the NIR photoactivities of Er^{3+}-doped Zn/Cu/Al-MPO with various photocatalysts in different references. However, even neglecting the much low power of 6.5 W LED used in this study, the NIR photocatalytic activity of Er^{3+}-doped Zn/Cu/Al-MPO is still much better than that of the most reported full-spectrum photocatalyst. To give a direct comparison between WS_2 and Er^{3+}-doped Zn/Cu/Al-MPO, their NIR photocatalytic activities were tested under the same conditions. The results were shown in Fig. S8.

Table S1 NIR photoactivity comparison among various reported full spectrum photocatalysts

Name of photocatalyst	NIR light resource	Amount of catalyst	Amount, concentration of MO	Removal rate /Irradiation time	References
Er^{3+}-doped Zn/Cu/Al-MPO	6.5 W 850 nm LED	20 mg	20 mL, 20 mg/L	91%/80 min	This study
Er^{3+}-doped Zn/Cu/Al-MPO	6.5 W 850 nm LED	20 mg	20 mL, 40 mg/L	88.5%/180 min	This study
[a] Cr_2O_3:P@f-P	300 W infrared lamp with filter glass	20 mg	100 mL,10 mg/L	Near 100%/300 min	H. Zhou et al., Nanoscale, 2017, **9**, 3196.
Ag_2S-50%/Ag_3PO_4	300 W infrared lamp with cutoff filter (λ≥760 nm)	35 mg	80 mL,10ppm	32%/240 min	J. Tian et al., Appl. Catal. B, 2017, **209**, 566.
RGO/Ag_2S/TiO_2	2 W 980 nm diode laser	10 mg	20 mL, 10 mg/L	56%/180 min	T. Liu et al., Appl. Catal. B, 2017, **204**, 593.
Ag_2S quantum dot/TiO_2 nanobelt	300 W infrared lamp with cutoff filter	20 mg	20 mL, 20 mg/L	71%/60 min	X. Hu et al., J. Ind. Eng. Chem., 2017, **45**, 189.
VS_4 sub-microspheres	300 W infrared lamp with filter glass	20 mg	20 mL, 20 mg/L	60%/120 min	Y. Zhou et al., J. Colloid Interface Sci., 2017, **498**, 442.
$Cu_{1.8}Se$/Cu_3Se_2 Composite	300 W xenon lamp with cutoff filter (λ≥800 nm)	100 mg	100 mL, 50 mg/L	75%/180 min	(L-N. Qiao et al., Nanomaterials **2017**, 7, 19
Au/Bi_2WO_6 nanosheets	250 W infrared lamp with cutoff filter (λ≥760 nm)	20 mg	20 mL, 20 mg/L	71% /120 min	X. Hu et al., ChemCatChem, 2017, **9**, 1511.
Ag_2O nanoparticle/TiO_2 nanobelt,	5 W 840 nm LED	10 mg	10 mL, 20 mg/L	65%/80 min	N. Wei et al., Appl. Catal. B, 2016, **198**, 83
[b]CNS-3	300 W xenon lamp with a cutoff filter (λ ≥ 760 nm)	100 mg	100 mL, 10 mg/L	70%/120 min	H. Wang et al., Appl. Catal. B, 2016, **193**, 36
α-$NaYF_4$:Yb,Tm@TiO_2/RGO	2 W 980 nm diode laser,	5 mg	5 ml, 15 ppm,	70%/720 min	W. Wang et al., Appl. Catal. B, 2016, **182,** 184.
TNFePc/BiOCl	300 W Xe lamp (λ≥ 600 nm)	100 mg	100 mL, 10 mg/L	Near 100%/180 min	L. Li et al., Dalton Trans., 2016, **45**, 9497
WS_2 Nanosheet	5W NIR LED light	50 mg	50 mL, 20 mg/L	80%/300 min	Y. Sang et al., Adv. Mater. **2015**, *27*, 363
In_2S_3 nanomaterials	250 W infrared lamp with cutoff filter (λ ≥ 720 nm)	20 mg	20 mL, 20 mg/L	67.2%/180 min	W. Gao et al., *Appl. Catal., B*, 2015, **176**, 83
H_xWO_3/WO_3	500 W Xe arc lamp (λ ≥ 760 nm)	50 mg	50 mL, 10 mg/L	25%/120 min	L. Zhang et al., Appl. Catal. B, 2015, **168,** 9

a Core-shell Structured Cr_2O_3:P@Fibrous-Phosphorus Hybrid Composites

b Sb_2S_3/ultrathin g-C_3N_4 sheets heterostructures embedded with g-C_3N_4 quantum dots

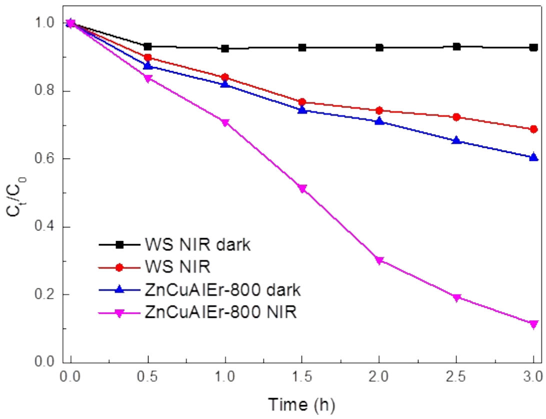

Fig. S8. Photocatalytic degradation of MO with a concentration of 40 mg/L in the presence of Er^{3+}-doped Zn/Cu/Al-MPO and WS_2, respectively in the dark and under NIR irradiation.

As shown in Fig. S8, the reported NIR photocatalyst WS_2 nanosheet has a lower absorption capacity for MO than Er^{3+}-doped Zn/Cu/Al-MPO, and can reach adsorption balance within 30 min even at the high MO concentration of 40 mg/L. However, the removal rate of MO by the WS_2 nanosheet is only 31.1% under NIR irradiation while the removal rate of MO by the Er^{3+}-doped Zn/Cu/Al-MPO is as high as 88.5% under the same experimental condition, indicating that the as-prepared Er^{3+}-doped Zn/Cu/Al-MPO has a much higher NIR photocatalytic activity.

8. FTIR spectra of as-prepared Zn/Cu/Al/Er-HLC and Er^{3+}-doped Zn/Cu/Al-MPO

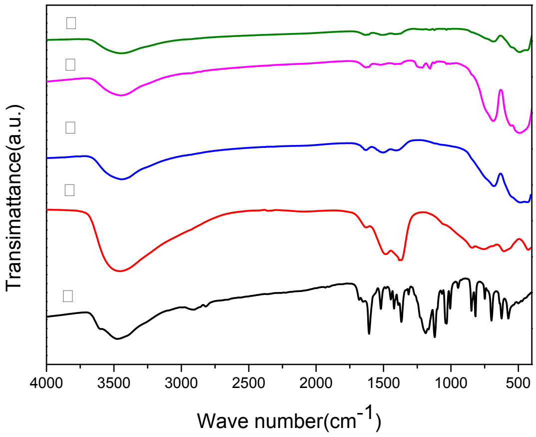

Fig. S9. FTIR spectra of (I) methyl orange, (II) Zn/Cu/Al/Er-HLC, (III) Er^{3+}-doped Zn/Cu/Al-MPO, (IV) Er^{3+}-doped Zn/Cu/Al-MPO after mixing with MO aqueous solution in the dark for 3 h, (V) Er^{3+}-doped Zn/Cu/Al-MPO after mixing with MO aqueous solution in the dark for 3 h followed by irradiating under near-infrared light for 8 h.

The FTIR spectrum of as-synthesized products and MO are shown in Fig. S9. In the spectra of MO as shown in curve I, the broad band at 2912.65 cm^{-1} is due to the asymmetric –

CH_3 stretching vibration, while the band at 1607.26 cm^{-1} comes from aromatic -C=C- bonds. The peak at 1419 cm^{-1} is assigned to –N=N- stretching vibration. The peak at 1367.5 cm^{-1} is for the C-N stretching vibration, in which the N is connected to aromatic ring. The peaks at 1119.78 cm^{-1} and 1191.17 cm^{-1} come from the vibration of sulfonic group. In the FTIR spectrum of Zn/Cu/Al/Er-HLC (curve II), the broad band centered at 3467 cm^{-1} is attributed to the stretching vibration of hydroxyl groups from the Zn/Cu/Al/Er-HLC and adsorbed water that is confirmed by the water bending vibration at 1619.5 cm^{-1}. The absorption peak at 1497.12 cm^{-1} is likely due to the asymmetric stretching vibration of interlayer carbonates which means the successive synthesis of HLC.

When Zn/Cu/Al/Er-LDH was transformed into Er^{3+}-doped Zn/Cu/Al-MPO by calcination at 800°C, the peak assigned to CO_3^{2-} virtually disappears (curve III). In the IR spectrum of Er^{3+}-doped Zn/Cu/Al-MPO after interacting with MO in the dark at room temperature for 3h, as shown in curve IV, weak adsorption peaks at 1609.3 cm^{-1}, 1217.6 cm^{-1}, 1160 cm^{-1} reveal the adsorption of MO. However, the peak positions have changed compared to that of free MO, which indicates that Er^{3+}-doped Zn/Cu/Al-MPO have strong adsorption effect to MO. However, after being illuminated for 8 h under NIR light, the adsorption peaks at 1609.3 cm^{-1}, 1217.6 cm^{-1} and 1160 cm^{-1} almost disappear, indicating that the decolorization of MO solution is due to the photodegradation of MO.

9. XRD patterns of pristine and recovered Er^{3+}-doped Zn/Cu/Al-MPO

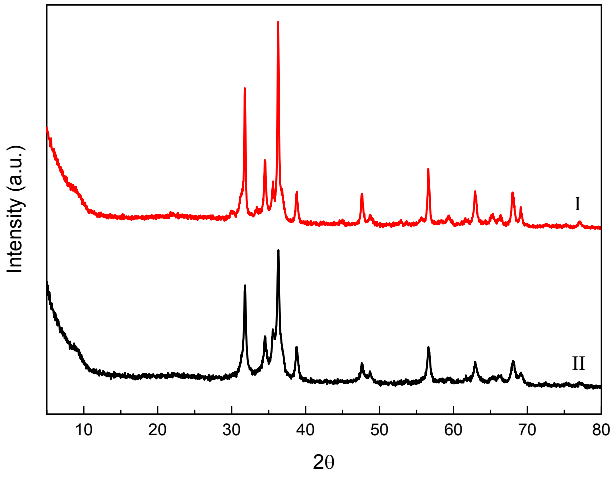

Fig. S10. XRD patterns of (I) pristine and (II) recovered Er^{3+}-doped Zn/Cu/Al-MPO

Fig. S10 shows the XRD patterns of pristine and recovered Er^{3+}-doped Zn/Cu/Al-MPO, which was obtained by directly drying at 60°C without any washing after 5 cycles of NIR photocatalytic experiments. As shown, the crystal structure of Er^{3+}-doped Zn/Cu/Al-MPO is not changed after it is cycled for five times unless the diffraction peaks assigned to Er_2O_3 disappear.

10. DRS of Er^{3+}-doped Zn/Al-MPO

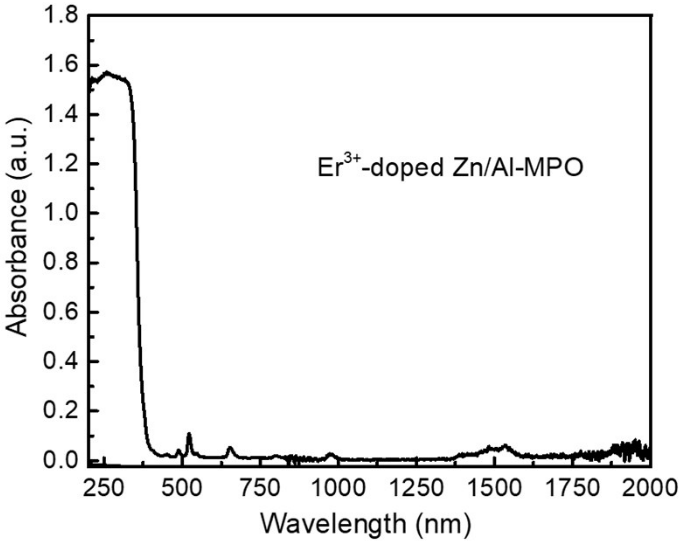

Fig. S11. DRS of Er^{3+}-doped Zn/Al-MPO

The optical absorption property of Er^{3+}-doped Zn/Al-MPO was analyzed using UV-Vis-NIR diffuse reflectance spectroscopy. As shown in Fig. S11, Er^{3+}-doped Zn/Al-MPO only has a strong absorption in UV region due to the absence of CuO.

References

1 S. Zhu, Y. Wu, T. Liu, X. Wang, J. Yan and A. Yin, *Int. J. Hydrogen Energy*, 2015, **40**, 5701.
2 S. Obregón, A. Kubacka, M. Fernández-García and G. Colón, *J. Catal.*, 2013, **299**, 298.
3 X. Yang, H. Xue, Q. Yang, R. Yuan, W. Kang and C. S. Lee, *Chem. Eng. J.*, 2017, **308**, 340.
4 X. Duan, D. Yuan and F. Yu, *Inorg. Chem.*, 2011, **50**, 5460.
5 W. Yao, S. Yu, Y. Zhou, J. Jiang, Q. Wu, L. Zhang and J. Jiang, *J. Phys. Chem. B*, 2005, **109**, 14011.
6 L. Zhu, Y. Liu, H. Zhang, H. Xiao and L. Guo, *Appl. Surf. Sci.*, 2014, **288**, 430.
7 Y. Su, B. Zhu, K. Guan, S. Gao, L. Lv, C. Du, L. Peng, L. Hou and X. Wang, *J. Phys. Chem. C*, 2012, **116**, 18508.
8 D. Li, W. Wang, D. Jiang, Y. Zheng and X. Li, RSC Adv., 2015, **5**, 14374.
9 H. Siddiqui, M.S. Qureshi, F.Z. Haque, *Optik*, 2014, **125**, 4663.